Programmable coherent linear quantum operations with high-dimensional optical spatial modes

Shikang Li,[1] Shan Zhang,[1] Xue Feng,[1,*] Stephen M. Barnett,[2]
Wei Zhang,[1] Kaiyu Cui,[1] Fang Liu,[1] and Yidong Huang[1]

[1] *Department of Electronic Engineering, Tsinghua University, Beijing 100084, China.*
[2] *School of Physics and Astronomy, University of Glasgow, Glasgow G12 8QQ, United Kingdom.*

(Dated: June 16, 2020)

A simple and flexible scheme for high-dimensional linear quantum operations is demonstrated on optical discrete spatial modes in the transverse plane. The quantum state tomography (QST) via symmetric informationally complete positive operator-valued measures (SIC POVMs) and quantum Fourier transformation (QFT) are implemented with dimensionality of 15. The statistical fidelity of SIC POVMs and fidelity of QST are ∼0.97 and up to 0.853, respectively, while the matrix fidelity of QFT is 0.85. We believe that our approach has the potential for further exploration of high-dimensional spatial entanglement provided by spontaneous parametric down conversion in nonlinear crystals.

I. INTRODUCTION

Photonics provides an outstanding platform for exploring non-classical computational resources [1] because entanglement can be conveniently generated through optical nonlinear effects [2–4], while linear manipulation protocols are available in multiple degrees of freedom [5–7]. Great efforts have been made to generate and manipulate high-dimensional entangled states, both for tests of quantum mechanics [8] and also for applications to quantum technology [9]. There is a push to increase the information encoded on a single photon [10] and achieve high-dimensional universal linear operation to extend the capacity of quantum processing as well as enhance the versatility of quantum computing and simulation [11].

High-dimensional quantum encoding has been demonstrated on photons exploiting the domains of optical path [12], frequency [4], temporal modes [13, 14] and transverse spatial modes [15–17]. For the first of these, Reck et.al, showed how arbitrary unitary operators could be realized using cascaded basic blocks consisting of phase modulators and couplers [5]. With the Reck scheme, programmable matrix operators and projectors with dimensionality from 6 to 26 [9, 12, 18, 19] have been reported in the path domain. However, only 6×6 arbitrary transformation matrix has been achieved while other demonstrations are fixed or partially adjustable due to the growing arrangement complexity of phase shifters and directional couplers. In the frequency domain, the quantum entanglement with Schmidt number up to 10 can be generated routinely through spontaneous four wave mixing (SFWM) [4], but the achieved dimensionality of quantum operator or projector is limited to 4 as ultra-fast electro optic modulation (EOM) devices are required [4, 7]. To exhibit substantial computational superiority, the dimensionality of fully tunable quantum operators has to be increased.

Transverse spatial modes provide abundant resources for quantum encoding and processing. Particularly, spatial mode entanglement induced by spontaneous parametric down conversion (SPDC) in nonlinear crystals [2, 3, 20–24] has been well investigated. Two photon spatial entanglement with high Schmidt number is potentially available with meticulously designed pump parameters [16, 17, 25]. However, the exploitation of such quantum resources has been hindered by the lack of universal operation protocols. The Reck scheme works well with one-dimensional in-plane path encoding, but is not compatible with these spatial encoded state in the two-dimensional transverse plane. Quantum operation protocols on orbital angular momentum (OAM), which can be considered as a specific basis of spatial modes, has been presented but only with limited dimensionality [6, 26]. Thus, although high-dimensional universal quantum operations on spatial modes could boost the exploration of currently existing entanglement resources, an efficient approach remains to be demonstrated.

Here, we tackle this issue by encoding the quantum information on the discrete coherent spatial (DCS) modes, and demonstrating a distinctive method to perform arbitrary linear quantum operators. In contrast with the in-plane path-encoding, DCS modes can be flexibly and arbitrarily arranged in the two-dimensional transverse plane according to the optical beam propagation so that more manageable manipulation can be achieved. Additionally, as our approach can be considered as the general form of path-encoding and transverse mode-encoding, the linear quantum operations on DCS modes would be compatible with both path-encoded qudits and spatial mode-encoded qudits. Furthermore, it is possible to combine our approach with that in the frequency domain since they are independent degrees of freedom. In this work, various quantum operators have been experimentally achieved with dimensionality up to 15×15, and we apply these to demonstrate symmetric informationally complete positive operator-valued measures (SIC

* Department of Electronic Engineering, Tsinghua University, Beijing 100084, China.; x-feng@tsinghua.edu.cn

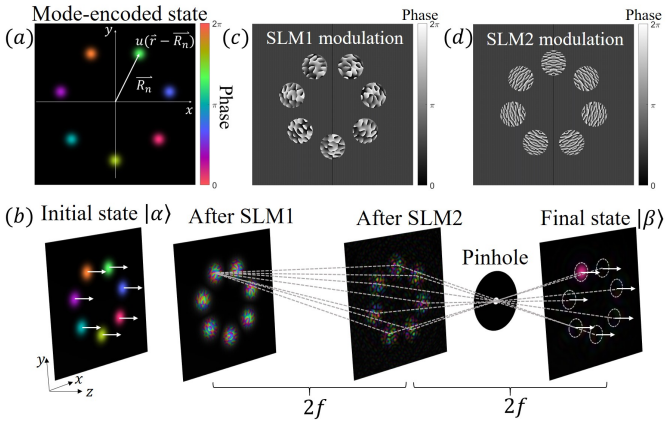

FIG. 1. (a) Definition of the discrete spatial modes. (b) Schematic setup for implementing linear quantum operators. A 7-dimensional QFT demonstration is shown as a concrete example. Simulated field evolutions after each SLM are presented. Phase modulation pattern implemented on SLM1(c) and SLM2 (d) for beam splitting and recombining, respectively.

POVMs) and quantum Fourier transform (QFT). This is, to the best of our knowledge, the implementation of discrete arbitrary linear quantum operators with the highest reported dimensionality [6, 7, 9, 12]. Due to the universality, precision, and controllability, our scheme makes possible high-dimensional demonstrations of nonclassical phenomena and quantum information processing. This can be achieved by exploring fully multipath entanglement in transverse plane, which can be provided by the whole spontaneous down-conversion cone [15] or integrated path-encoded photonic qudits with the help of 3D waveguide coupling [27].

II. PRINCIPLE

Generally, with a set of well-defined orthogonal basis states, any linear operation can be expressed as $|\beta\rangle = T|\alpha\rangle$, in which T is a complex matrix and $|\alpha\rangle$ and $|\beta\rangle$ are initial and final state vectors in a complex vector space with dimensionality of N. In our previous works [28, 29], the state vector of $|\alpha\rangle$ and $|\beta\rangle$ was encoded on a set of DCS modes $|\varphi_n\rangle = u(\boldsymbol{r}-\boldsymbol{R}_n)$. As indicated in Fig. 1(a), $\boldsymbol{R}_n$ is the transverse coordinate of the n-th DCS mode while $u(\boldsymbol{r}-\boldsymbol{R}_n)$ is considered as a Gaussian function of $u(\boldsymbol{r}-\boldsymbol{R}_n) \propto \exp(-|\boldsymbol{r}-\boldsymbol{R}_n|^2/{w_0}^2)$ and the optical waist of w_0 is designed as sufficiently small compared with transverse distance $|\boldsymbol{R}_n-\boldsymbol{R}_m|$ between two adjacent DCS modes to ensure the orthogonality [29]. Hence the state vector can be expressed as $|\alpha\rangle = \sum a_n|\varphi_n\rangle$.

For a given linear operator of T, one-to-N beam splitting and N-to-one beam recombining are required to achieve the columns and rows of a general transformation matrix. T should be decomposed as the Hadamard product of two matrices ($T_{mn} = A_{mn}B_{mn}$). The optimal

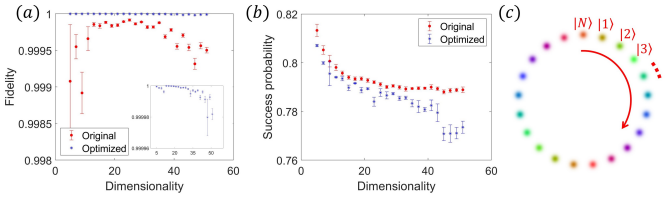

FIG. 2. Simulated fidelity (a) and success probability (b) for one-to-N beam splitting. (c) The transverse coordinates of employed spatial modes are arranged on a circle.

decomposition to achieve maximum success probability has been discussed in our previous work [29]. With the obtained matrices of A and B, beam splitting and recombining can be implemented by two phase-only spatial light modulators (SLM1 and SLM2) combined with two $2f$ systems and a pinhole (Fig. 1(b)). Considering a diffraction grating illuminated by an optical beam, the diffraction pattern on the Fourier plane of a diffraction grating is the convolution of Fourier coefficients of diffraction grating and Fourier spectrum of the incident beam field according to diffraction theory [30]. Thus, the diffraction gratings on SLM1 and SLM2 are set according to the Fourier coefficients of A_{mn} and B_{mn}:

$$\begin{cases} H_{1n}(\boldsymbol{r}) = \exp(i\arg\{\sum_{m=1}^{N}\mu_{mn}A_{mn} \\ \qquad\qquad \exp[i\boldsymbol{k}_{mn}\cdot(\boldsymbol{r}-\boldsymbol{R}_n)]\}) \\ H_{2m}(\boldsymbol{r}) = \exp(i\arg\{\sum_{n=1}^{N}\nu_{mn}B_{mn} \\ \qquad\qquad \exp[-i\boldsymbol{k}_{mn}\cdot(\boldsymbol{r}+\boldsymbol{R}_m]\}), \end{cases} \tag{1}$$

where $\boldsymbol{k}_{mn}$ is transverse wave vector expressed as $\boldsymbol{k}_{mn} = k(\boldsymbol{R}_n-\boldsymbol{R}_m)/2f$. Two sets of optimization coefficients of $\{\mu_{mn}\}$ and $\{\nu_{mn}\}$ are introduced to achieve desired beam splitting and recombining ratio. The detailed modulation functions on SLMs are included in appendix A. As a concrete example, the diffraction gratings for 7-dimensional QFT are displayed in Fig. 1(c) and (d).

We choose the same optimization algorithm as employed in [31]. The fidelity between target and implemented matrix (A or B *vs.* $A_{\rm exp}$ or $B_{\rm exp}$) normalized by energy [32] is optimization target.

$$\mathrm{Fide}(A_{\rm exp}, A) = \left|\frac{\mathrm{Tr}(A^\dagger A_{\rm exp})}{\sqrt{\mathrm{Tr}(A_{\rm exp}^\dagger A_{\rm exp})\cdot\mathrm{Tr}(A^\dagger A)}}\right|^2. \tag{2}$$

In Fig. 2, Huygens-Fresnel simulation results for beam splitting of dimensionality up to 51 are summarized. Each data point is the statistical combination of 20 random complex target matrices. The data labeled as "Original" correspond to $\{\mu_{mn}\}\equiv 1$ without any optimization, while near ideal fidelity values could be achieved with small reduction ($< 2\%$) of success probability after optimization. We believe that the imperfection is caused by a calculation error arising from iteration tolerance. The success probability is calculated from $P(A_{\rm exp}, A) = \mathrm{Tr}(A_{\rm exp}^\dagger A_{\rm exp})/\mathrm{Tr}(A^\dagger A)$. Similar simulation results have

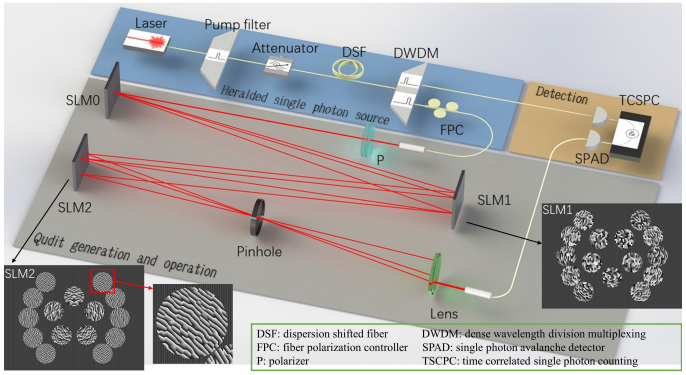

FIG. 3. Experimental setup. Insets, modulation functions on SLM1 and SLM2, together with an enlarged figure of a typical phase grating.

been obtained with N-to-one beam recombining. The overall fidelity considering both beam splitting and recombining is approximately the square value of those plotted in Fig. 2. As shown in Fig. 2(c), the transverse coordinates of our proposed discrete spatial modes are arranged on a circle during these simulation to mimic the spatially sampled Type-I SPDC cone.

III. RESULTS

Experiments have been performed to verify and evaluate our scheme. Figure. 3 illustrates the experimental setup, in which, the heralded single photon source and time correlated single photon counting (TCSPC) are employed. A pulsed laser (Alnair PFL200) with central wavelength of ∼1552 nm serves as degenerate pump to generate SFWM in dispersion shifted fiber (DSF)[33]. The temperature of DSF is cooled to 77 K with liquid nitrogen to reduce the Raman scattering noise. The time correlated signal and idler photons are filtered out by dense wavelength division multiplexing (DWDM) filters. The idler photons (1555.7 nm) are directly collected by InGaAs single photon detector (IDQ220), which heralds the detection of signal photon (1549.3 nm) after linear operation. The signal photons are collimated to a free space Gaussian mode expressed as $|\varphi_0\rangle$ under DCS mode basis $|\varphi\rangle\langle\varphi|$. A beam splitter noted as $|\alpha\rangle\langle\varphi_0|$ is programmed on an additional spatial light modulator (Holoeye Pluto) labeled SLM0 to generate the initial qudit state $|\alpha\rangle = \sum a_n|\varphi_n\rangle$. The target operation $|\beta\rangle = T|\alpha\rangle$ is performed by SLM1 and SLM2 (operating in the reflection mode). The projection values of final state in the DCS mode basis after the quantum operation, $|\langle\varphi_n|\beta\rangle|^2$, are detected by a single photon avalanche detector (SPAD) with mono-mode fiber coupler one-by-one. Different spatial distribution of DCS modes (inset of Fig. 3) from simulation (Fig. 2(c)) is chosen to fully utilize the spatial area of SLMs and show the flexibility of our scheme. Actually, the spatial distribution of DCS modes could be properly designed and settled according to the applied single photon source or entanglement source. Particularly, the SLM0 could be replaced by SPDC for future bi-photon entanglement experiment, and the spatial sampling of SPDC cone as well as beam splitting could be done simultaneous by SLM1.

Quantum state tomography (QST) provides a full description of the quantum state [34]. Firstly, a 15-dimensional QST is performed to present the ability of arbitrary coherent matrix operation with our proposal. In experiments, symmetric informationally complete positive operator-valued measures (SIC POVMs) are employed. A SIC POVM basis $|\Psi_{jk}\rangle\langle\Psi_{jk}|$ can be generated by applying N^2 displacement operators [35] on a fiducial vector $|f\rangle$ [36]:

$$|\Psi_{jk}\rangle = \exp\left(\frac{2jk\pi i}{N}\right)\sum_{m=0}^{N-1}|\mathrm{mod}(k+m,N)\rangle\langle m|f\rangle. \quad (3)$$

QST was performed using a compressed sensing method [37], employing 100 randomly selected SIC POVMs from the 225 distinct elements. Fig. 4 presents two sets of experimental results according to the representative eigenstate $|\varphi_4\rangle$ and superposed state $|\omega_2\rangle$ with the definition:

$$|\omega_n\rangle = N^{-1/2}\sum_{d=1}^{N}\exp\left[-\frac{2\pi i(d-1)n}{N}\right]|\varphi_d\rangle. \quad (4)$$

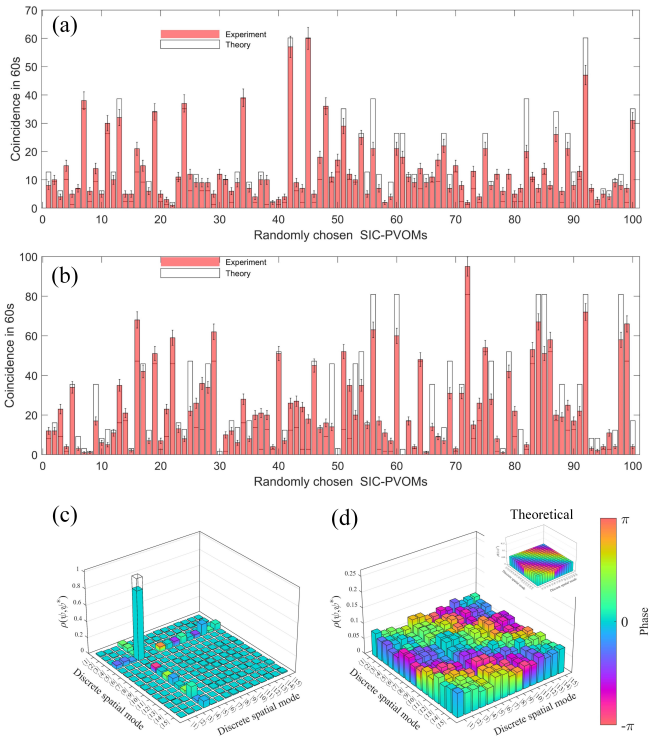

FIG. 4. Quantum state tomography via compressed sensing method. (a) and (b) Projective measurements. (c) and (d) Reconstructed density matrices.

The expectation values of projective measurements for such two states are displayed in Fig. 4(a) and (b), where the filled and empty histograms indicate experimental recorded coincidence counts in 60 seconds and theoretical calculated references, respectively. The implementation accuracy is evaluated by statistical fidelity values, which is defined as $F_s(p_{exp}, p) = \sum \sqrt{p_{exp} \cdot p}$ [38], between theoretical and experimental probability distributions corresponding to the histograms in Fig. 4(a) and (b). The fidelity values of these two datasets are found to be 0.98 and 0.96. The density operators reconstructed from the randomly chosen SIC POVMs are plotted in Fig. 4(c) and (d). The theoretical density matrices are displayed as empty bars in Fig. 4(c) and inset in Fig. 4(d). The fidelity of density matrix is evaluated with the formula [39]:

$$Fide(\rho_{\text{exp}}, \rho) = \left| Tr\sqrt{\sqrt{\rho}\rho_{\text{exp}}\sqrt{\rho}} \right|^2, \tag{5}$$

where ρ_{exp} and ρ are reconstructed and reference density matrices, respectively. The fidelity values are 0.853 and 0.815 for the eigenstate $|\varphi_4\rangle$ and the superposition state $|\omega_2\rangle$, respectively. It is convenient to implement complex operators in our scheme, allowing the reconstruction of a complicated density matrix with 225 nonzero complex elements. Further to the results shown in Fig. 4, another three similar experiments were performed. The averaged fidelity value is found to be 0.97 ± 0.02 among a total of 500 experimentally generated 15-dimensional projective operators randomly chosen from SIC POVMs. These projective operators in Eq. (3) exhibit various amplitude and phase distributions. These results suggest that our method is valid for arbitrary linear quantum operations up to 15 dimensions and it is the first implementation of SIC POVMs on 15-dimensional photonic qudits to the best of our knowledge [35].

The required number of projective measurements can be greatly reduced by using a compressed sensing technique. However, the reconstruction uncertainties would increase by a factor that has a negative correlation with sampling ratio [37]. Figure. 5 illustrates the measured fidelity and trace distance of the reconstructed density matrices versus sampling ratio. Statistical results of 5 experimental data sets are plotted. The trace distance is calculated as $T(\rho_{\text{exp}}, \rho) = \text{Tr}\left[\sqrt{(\rho_{\text{exp}} - \rho)^\dagger(\rho_{\text{exp}} - \rho)}\right]/2$. As the generated states under test are nearly pure, the trace distance is close to the upper bound of $\sqrt{1 - \text{Fide}(\rho_{\text{exp}}, \rho)^2}$.

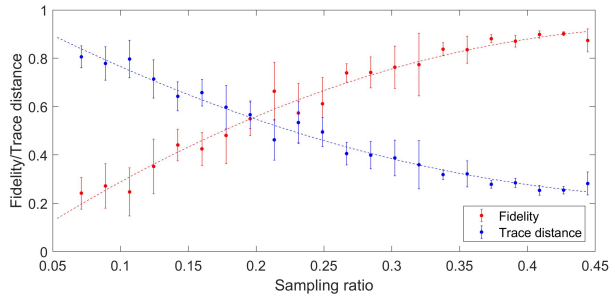

FIG. 5. Fidelity and trace distance for our reconstructed density matrix versus sampling ratio.

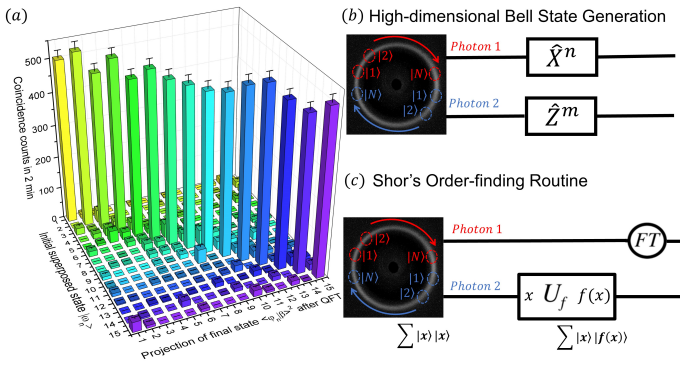

FIG. 6. QFT with dimensionality of 15×15 tested with the conjugate Fourier basis. (b) Illustration for high-dimensional Bell states generation. (c) Equivalent order-finding routine with high-dimensional entangled photons. $f(x) = 2^x \pmod N$ denotes modular exponential. Inset, type I SPDC cone photographed by near-infrared CMOS camera.

Next, a 15×15 QFT was performed, which is an important unitary quantum operation in quantum information processing such as Shor's factorization algorithm [40]. The phase components in experimental QFT matrix F_{exp} (with the target QFT matrix labeled F) could not be measured directly in the computational basis $|\varphi\rangle\langle\varphi|$, thus the fidelity value of QFT is evaluated in the conjugate Fourier basis $|\omega\rangle\langle\omega|$ as defined in Eq. (4).

If the initial state $|\omega_n\rangle$ is prepared precisely, then $F|\omega_n\rangle = |\varphi_n\rangle$. Due to the orthogonal nature of conjunctive Fourier basis that $|\langle\omega_i|\omega_j\rangle|^2 = \delta_{ij}$, the fidelity value between experimental and theoretical QFT matrices can be expressed as $\text{Fide}(F_{\text{exp}}, F) = \text{Fide}(F_{\text{exp}}\Omega, F\Omega)$, where Ω is a matrix whose n-th column is $|\omega_n\rangle$. In theory, $F\Omega$ is the identity matrix acting in the computational basis $|\varphi\rangle\langle\varphi|$ and so $F_{\text{exp}}\Omega$ should approximate the identity if F_{exp} is sufficiently close to F. The experimental results for $F_{exp}\Omega$ are displayed in Fig. 6(a), which consists of coincidence counts in 120 seconds. The error bars are one standard deviation estimated from Poissonian counting statistics. The fidelity is calculated as 0.85 ± 0.02. The deviation from unit fidelity is caused mainly by dark count rates of the SPADs and the calibration error of the experimental setup (see error analysis in appendix B). After meticulous phase calibration (explained in appendix A 2), the fidelity values reach $0.93 \sim 0.99$ with stability of 7 days for coherent light source and the corresponding experimental data are included in appendix C.

IV. EXTENSION TO PHOTON PAIRS

In this work we have concentrated only on single-photon operations, with each photon generated by heralding from a spontaneous parametric process. It should be possible to extend our methods to manipulate both photons in an entangled pair generated from this source and so to realise high-dimensional Bell states and order-finding routines as indicated in Figs 6(b) and 6(c). Our investigations suggest that it should be possible to generate and manipulate such states with a large Schmidt number of $K \sim 40$ [16]. The spatial entangled state $\sum |x\rangle|x\rangle$ is one of the high-dimensional generalized Bell-states. By acting on this with a high-dimensional $\hat{X}$ gate on one photon and a corresponding $\hat{Z}$ gate on its partner, the Bell-state can be switched to any another, for applications such as quantum teleportation of qudits [41]. Two-photon gates employed in linear optical quantum information processing are non-deterministic in nature [11]. For this reason we propose an alternative procedure for the order-finding routine in Shor's factorization algorithm. This scheme, which avoids two-photon operations, is depicted in Fig. 6(c). High-dimensional QFT and compiled modular exponential [42] are applied on twin beams from SPDC, respectively. The optical nonlinear process could provide a large enough state space for further demonstration [25]. Furthermore, our scheme is also available for indistinguishable multi-photon manipulation including boson sampling [18].

We begin our discussion with an analysis of the extent to which the distinct paths in our scheme are distinguishable. The optical path differences induced during propagating from SLM1 to SLM2 are compensated in Eq. (A6). The phase compensation is valid when the coherence length of photons is larger than the optical path differences. In this demonstration, the distance between SLM1 and SLM2 is 0.8 m, while the maximum and average distances between DCS modes in transverse plane are ∼5 mm and ∼1 mm, respectively. This leads to a maximum optical path difference of ∼20 times of optical wavelength ($30\mu m$ 0.1ps) and an average optical path difference of about one wavelength. The influences of optical path differences will be sufficiently small when the linewidths of the pump filter and signal (idler) filter are much narrower than 10THz (1/0.1ps). Thus, our scheme is available for indistinguishable multi-photon manipulation including boson sampling [18].

When the transverse coordinates of spatial encoding basis are considered as distributed on one single circle, the two-photon spatial-entangled state generated via frequency-degenerate type-I SPDC can be expressed as $\sum_{x=0}^{N-1} |x\rangle|x\rangle$. This is a consequence of transverse momentum conservation or phase matching in the source crystal and we note that N should not exceed the Schmidt number K of the transverse momentum entanglement. According to [16], a closed form of Schmidt number is:

$$K = \frac{1}{4}\left(b\sigma + \frac{1}{b\sigma}\right)^2, \tag{6}$$

where σ and b^{-1} are width of Gaussians. For the biphoton amplitude distribution of type-I SPDC cone shown in the main text, the amplitudes of b^{-1} and σ are proportional to the radius and thickness of SPDC cone, respectively. With this estimation, the Schmidt number for our SPDC source is $K \sim 40$ and this sets a limit on the dimensionality achievable in our future experiments. We present two experimental proposals for our linear operation scheme and entangled photon source.

A. Compiled demonstration of Shor's factorization algorithm

The difficulty in factoring a composite number $M = pq$ is believed to be equivalent to that of finding the period r of the modular exponential function (MEF) of $f(x) = a^x \pmod M$, where number a can be chosen to be any integer. Shor's algorithm provides an efficient routine [38–40, 42, 45] to find the period r, where the "quantum parallelism" can be achieved by coherent manipulation and detection of the highly entangled state:

$$\frac{1}{\sqrt{N}} \sum_{x=0}^{N-1} |x\rangle|\mathrm{mod}(a^x, M)\rangle. \tag{7}$$

The value of N denotes the size of each quantum register set. We proceed by applying the quantum Fourier transformation (QFT) of dimensionality N to the first register, which produces quantum interference from which information about period r of $f(x)$ can be deduced [42]:

$$\frac{1}{N} \sum_{y=0}^{N-1} \sum_{x=0}^{N-1} e^{2\pi i x y/N} |y\rangle|\mathrm{mod}(a^x, M)\rangle. \tag{8}$$

Thus, the preparation of state in Eq. (8) is an essential element for demonstrating Shor's algorithm.

The initial states of two quantum registers are separable ground states in the original order-finding routine [40]. The state in Eq. (7) may be realised by multiphoton execution that entangles N input value of x in first register with corresponding value $f(x)$ in the second register. However, with initial entangled state $\sum_{x=0}^{N-1} |x\rangle|x\rangle$ at our proposal, there is no need for generating entanglement with multiphoton controlled gates, which would lead to low success probability with post selection [11]. Instead, we proceed by acting with the QFT on the first quantum register to produce the state

$$\frac{1}{N} \sum_{y=0}^{N-1} \sum_{x=0}^{N-1} e^{2\pi i x y/N} |y\rangle|x\rangle. \tag{9}$$

We recognise this transformation as one of our linear operators applied to the first photon. Next, the MEF is applied on the second quantum register. Thus, the state in Eq. (8) is prepared and the quantum parallelism could be exhibited by simultaneously readout of two registers. Though MEF is nonlinear operation and could not be implemented directly with any linear operation scheme, a proof-in-principle experiment of Shor's algorithm would be feasible with linear transformation performing the precompiled MEF [42]. As a concrete example, with $N = 16$ for number of sampling on SPDC cone and the dimensionality of QFT, the factorization of $15 = 3 \times 5$ could be demonstrated. Additionally, such an implementation would not be limited to the "easy" case [42, 46] of $a = 11$, that has been previously reported with photonic platform.

It is significant that high-dimensional entangled state is employed as the initial state, thus multiphoton controlled gates are avoided. Due to the high-dimensional encoding, only one photon is needed for each quantum register, thus the coherent manipulation and detection could be further simplified.

B. Generation of complete high-dimensional Bell basis

The complete high-dimensional Bell basis can be generated using our technique. The N-dimensional Bell basis can be written as [41, 47]:

$$|\psi\rangle_{mn} = \frac{1}{\sqrt{N}} \sum_{x=0}^{N-1} e^{2\pi i x n/N} |x\rangle |\mathrm{mod}(x+m, N)\rangle. \quad (10)$$

We begin with the initial state sampled from the SPDC cone, we have one of the N-dimensional Bell states:

$$|\psi\rangle_{00} = \frac{1}{\sqrt{N}} \sum_{x=0}^{N-1} |x\rangle |x\rangle. \quad (11)$$

With N-dimensional shift matrices and clock matrices applied to the second photon, the Bell state of $|\psi\rangle_{00}$ can be transformed into $|\psi\rangle_{m0}$ and $|\psi\rangle_{0n}$, respectively. Here, shift matrices and clock matrices have the forms:

$$T_{\mathrm{shift,m}} = \frac{1}{\sqrt{N}} \sum_{x=0}^{N-1} |\mathrm{mod}(x+m, N)\rangle\langle x|, \quad (12)$$

$$T_{\mathrm{clock,n}} = \frac{1}{\sqrt{N}} \sum_{x=0}^{N-1} e^{2\pi i x n/N} |x\rangle\langle x|. \quad (13)$$

The state of $|\psi\rangle_{00}$ can then be transformed into any target Bell state $|\psi\rangle_{mn}$ by applying a product of $T_{\mathrm{shift,m}}$ and $T_{\mathrm{clock,n}}$ to the second photon. Thus, the complete N-dimensional Bell basis can be generated by type-I SPDC combined with our linear operation scheme. Furthermore, unit success probability can be achieved, at least in principle, when performing shift matrices and clock matrices, as well as any of their products. As a concrete example, 15-dimensional complete Bell basis could be generated with our proposed 15×15 arbitrary matrix transformations. As the maximally entangled two-particle quantum states, the complete Bell basis could be employed for high-dimensional quantum protocols such as teleportation, dense coding, and entanglement swapping.

V. DISCUSSION AND CONCLUSIONS

Our results can be compared with recent developments using multi-plane light conversion [26, 43]. We note that using our method we have been able to work with a significantly higher dimension of state space. Moreover, we have avoided a cascaded structure and, with it, the requirement for an increase in the number of elements as the dimensionality increases, albeit with a penalty is success probability.

Before summarizing, we would like to provide some details on the success probability, reliability and dimensionality about our scheme. A probability factor of $1/N$ is incurred in the spatial filtering by the pinhole in the worst case of an $N \times N$ demonstration as previously discussed [29]. The intrinsic loss is determined by the average number of nonzero elements in each row of target matrix. Our scheme would be lossless for $\hat{X}$ gates and $\hat{Z}$ gates that could be used to construct any unitary transformations [6]. In the 15×15 QFT demonstration, the total insertion loss was measured to be 21.2 dB. This arises from the theoretical loss of ∼13.7 dB, estimated by the $1/N$ factor, imperfect success probability of phase gratings shown in Fig. 2(b), and an additional loss of 7.5 dB due to the modulation efficiency and reflection rate of two SLMs.

The intrinsic loss of $1 - 1/N$ is the inevitable penalty paid in order to avoid a cascaded structure. Against this, for our simple non-cascading structure, the attenuation induced by the optical elements should be largely independent of the dimensionality of linear operator realized. Moreover, our scheme exhibits robustness against phase modulation errors compared with a cascaded design [29].

The quantum operators realized here were demonstrated with dimensionality of 15, but an extension of the 24-dimensional arbitrary linear transformation has been demonstrated previously [29]. In principle the achievable dimensionality is only limited by the achievable spatial resolution of phase modulation. Our method is not limited by SLMs. Any passive holographic elements able to perform the phase modulation would be possible including, for example, specially engineered metasurfaces [44]. Thus, it should be possible to realise on-chip high-dimensional quantum operator with our scheme.

In summary, we have proposed and demonstrated a simple and flexible scheme to perform arbitrary linear quantum operators with high fidelity and high dimen-

sionality. SIC POVMs and QFT have been performed with dimensionality of 15×15. Since the DCS modes are employed, we believe that our work would be potential to fully explore SPDC on high-dimensional quantum applications including Bell-states switching and also compatible for operating the well-investigated path-encoded qudits.

ACKNOWLEDGMENTS

This work was supported by the National Key Research and Development Program of China (2017YFA0303700, 2018YFB2200402), the National Natural Science Foundation of China (Grant No. 61875101 and 61621064), Beijing Innovation Center for Future Chip and Beijing academy of quantum information science. SL would like to thank Peng Zhao, Xin Yao and Rong Xue for their valuable discussions and helpful comments. In addition, SMB thanks the Royal Society for support through the grants RP/150122 and RP/EA/180010.

Appendix A: Spatial light modulators encoding method

The spatial resolution of the employed spatial light modulator (SLM, Holoeye Pluto series) is 1920×1080, while the size of each single pixel is about $8\mu m \times 8\mu m$. Firstly, we would like to introduce some ancilliary phase modulation patterns to simplify the following explanation.

1. Phase modulation functions

As mentioned in the main text, the modulation efficiency of SLMs is less than unity. To separate effectively the components directly reflected without modulation, first order diffraction is employed, and the function of phase modulation is

$$F_{\text{grating}}(\boldsymbol{r}) = \exp(i\boldsymbol{k}_{\text{grating}} \cdot \boldsymbol{r}). \tag{A1}$$

With the help of such blazed gratings, the directly reflected components can be spatially filtered out. In this work, the transverse wave vector $\boldsymbol{k}_{\text{grating}}$ is selected to obtain blazed grating with a spatial period of 4 pixels.

To maintain the transverse size of Gaussian spots against natural divergence during propagation, a symmetric confocal cavity is implemented between SLM1 and SLM2 by Fresnel lens programmed on SLMs. Under the paraxial approximation, the transmission function of a lens with a focal length of f is

$$F_{\text{lens}}(\boldsymbol{r}) = \exp\left(\frac{ik|\boldsymbol{r}|^2}{2f}\right). \tag{A2}$$

Additionally, a binary function is employed to avoid spatial coincidences of phase gratings acting on different Gaussian spots $|\varphi_n\rangle$. The expression is

$$\chi(\boldsymbol{r}) = \begin{cases} 1, & |\boldsymbol{r}| < R_{\text{threshold}} \\ 0, & \text{elsewhere.} \end{cases} \tag{A3}$$

The value of $R_{\text{threshold}}$ is determined according to the beam waist of a single Gaussian spot. The amplitude modulation is implemented by a checker-board method. The phase modulation settled on SLM0 is

$$\begin{aligned} F_{\text{diff0}}(\boldsymbol{r}) = &\exp\left\{ i \arg\left[\sum_{n=1}^{N} \xi_n a_n \exp(i\boldsymbol{k_n} \cdot \boldsymbol{r}) \right] \right\} \\ &\cdot F_{\text{lens}}(\boldsymbol{r}) \chi(\boldsymbol{r}) F_{\text{grating}}(\boldsymbol{r}), \end{aligned} \tag{A4}$$

where $\{a_n\}$ is the state vector of the initial state, and $\{\xi_n\}$ are optimization parameters to ensure desired beam splitting. The transverse wave vectors of $\{\boldsymbol{k}_n\}$ determine the propagation directions of initial Gaussian spots and they are utilized to mimic the spontaneous parametric down conversion cones produced in a nonlinear crystal. Under the paraxial approximation, the definition of $\{\boldsymbol{k}_n\}$ is

$$\boldsymbol{k}_n = \frac{k\boldsymbol{R}_n}{2f} \qquad \forall n = 1, \cdots, N. \tag{A5}$$

The transverse coordinates of the n-th Gaussian spot is $\boldsymbol{R}_n$ as mentioned in the main text. The phase modulation on SLM1 is chosen to be

$$\begin{aligned} F_{\text{diff1}}(\boldsymbol{r}) = \sum_{m=1}^{N} \exp &\left[i \arg\left(\sum_{n=1}^{N} \mu_{mn} A_{mn} \right.\right. \\ &\left.\left. \cdot \exp[i(\boldsymbol{k}_{mn} - \boldsymbol{k}_m) \cdot (\boldsymbol{r} - \boldsymbol{R}_m) - i\theta_{mn}] \right) - i\delta_m \right] \\ &\cdot F_{\text{lens}}(\boldsymbol{r} - \boldsymbol{R}_m) \chi(\boldsymbol{r} - \boldsymbol{R}_m) \cdot F_{\text{grating}}(\boldsymbol{r}). \end{aligned} \tag{A6}$$

The parameters of μ_{mn}, A_{mn} and $\boldsymbol{k}_{mn}$ in Eq. (A6) have the same definitions as those in the main text. As the optical path of each spot is different during propagating from SLM1 to SLM2, the phase compensation of θ_{mn} should also be different for each splitting direction and can be expressed as

$$\theta_{mn} = \frac{k|\boldsymbol{R}_n - \boldsymbol{R}_m|^2}{4f}. \tag{A7}$$

Similarly, a different phase compensation of δ_m is employed for each initial Gaussian spot to compensate for the path difference during propagating from SLM0 to SLM1. The value of δ_m is selected to be

$$\delta_m = \frac{k|\boldsymbol{R}_m|^2}{4f}. \tag{A8}$$

In addition to beam splitting and the focusing lens, extra beam refraction functions are also employed in Eq. (A6) to compensate for the initial transverse wave vectors $\{\boldsymbol{k}_n\}$ associated with each individual Gaussian spots generated by SLM0.

The function of SLM2 is beam recombining. This is the reverse procedure of beam splitting, and so the phase modulation functions are similar to those on SLM1. The phase modulation required on SLM2 is

$$F_{\text{diff2}}(\boldsymbol{r}) = \sum_{m=1}^{N} \exp\left[i \arg\left(\sum_{n=1}^{N} \nu_{mn} B_{mn} \cdot \exp[-i\boldsymbol{k}_{mn} \cdot (\boldsymbol{r} - \boldsymbol{R}_m)] \right) \right] \cdot F_{\text{lens}}(\boldsymbol{r} - \boldsymbol{R}_m)\chi(\boldsymbol{r} - \boldsymbol{R}_m) \cdot F_{\text{lens}}(\boldsymbol{r}) F_{\text{grating}}(\boldsymbol{r}). \tag{A9}$$

The parameters of ν_{mn}, B_{mn} and $\boldsymbol{k}_{mn}$ in Eq. (A9) have the same definition as those in the main text. In contrast with the phase modulation on SLM1, there is no need for extra additional refraction and phase compensation on SLM2, but an extra lens is required for the last step, which is beam filtering with a pinhole. A pinhole with transmission function described by $\chi(\boldsymbol{r})$ is positioned one focal length of f after SLM2. To accomplish beam filtering, a lens with focal length of f is placed at one focal length away after pinhole, as presented in the experimental setup in main text.

2. Phase calibration method

In the laboratory implementation, phase errors arise from the misalignment of optical elements. In addition, there would be extra phase errors if the phase compensation terms in Eq. (A6) are not estimated precisely. Fortunately, these phase errors are constant and independent of the target matrices. Thus, the phase errors can be corrected before the experiments are performed. The amplitudes of matrix elements are robust against misalignments and there is no need for amplitude calibration in most situations.

The phase calibration is performed with a laser source (RIO ORION) centered at 1550 nm in place of the heralded single photon source in experimental setup. The final state after linear operation is measured by a charge coupled device (CCD) camera. Generally, the influences of constant phase error ϵ on the implemented matrix transformation T^{real} turn out to be

$$T_{mn}^{\text{real}} = T_{mn} \exp(i\epsilon_{mn}). \tag{A10}$$

The error matrix $\exp(i\epsilon_{mn})$ is measured so that the phase errors can be compensated by implementing $T_{mn}\exp(-i\epsilon_{mn})$ rather than T_{mn}. Any matrix with no zero elements could be adopted for phase calibration. In our experiments, the discrete Fourier transformation (DFT) is performed without phase calibration at first. Then, the phase terms of all elements in the realized DFT are measured. Finally, the error matrix $\exp(i\epsilon_{mn})$ is deduced by comparing the achieved DFT and the standard DFT. A tomographic method is employed to measure the phase terms. By measuring the amplitudes of output vectors corresponding to meticulously designed input vectors, the phase terms of transformation matrix could be deduced. Here, the principle of calibration is shown with an example of 3×3 matrix.

$$\begin{bmatrix} O_{11} & O_{12} & O_{13} & O_{14} \\ O_{21} & O_{22} & O_{23} & O_{24} \\ O_{31} & O_{32} & O_{33} & O_{34} \\ O_{41} & O_{42} & O_{43} & O_{44} \end{bmatrix} = T_{3\times3}^{\text{real}} \times \begin{bmatrix} 1 & 1 & i & i \\ 1 & 0 & 1 & 0 \\ 0 & 1 & 0 & 1 \end{bmatrix}. \tag{A11}$$

The interference results of matrix elements in first column with elements in other columns are available as the intensities in output vectors. To calculate the relative phase with respect to elements in first column precisely, the inner product is performed twice. For example, the phase of T_{12}^{real} can be found from

$$\begin{aligned} I_{12}^{\cos} &= |O_{11}|^2 = |T_{11}^{\text{real}} + T_{12}^{\text{real}}|^2 \\ I_{12}^{\sin} &= |O_{13}|^2 = |iT_{11}^{\text{real}} + T_{12}^{\text{real}}|^2. \end{aligned} \tag{A12}$$

As the amplitudes of elements in T^{real} are known, the relative phases can be deduced from Eq. (A12) without any ambiguity. Generally, $2(N-1)$ tests with different input vectors are required to measure all the relative phase terms of the $N \times N$ matrix.

There would be, however, a constant relative phase between different rows of matrix that is not calibrated. These relative phase terms can be considered as path differences from each output port of the transformation to its corresponding detector. Thus, these phase terms have no influence in quantum computational tasks, including multiphoton interference such as boson sampling.

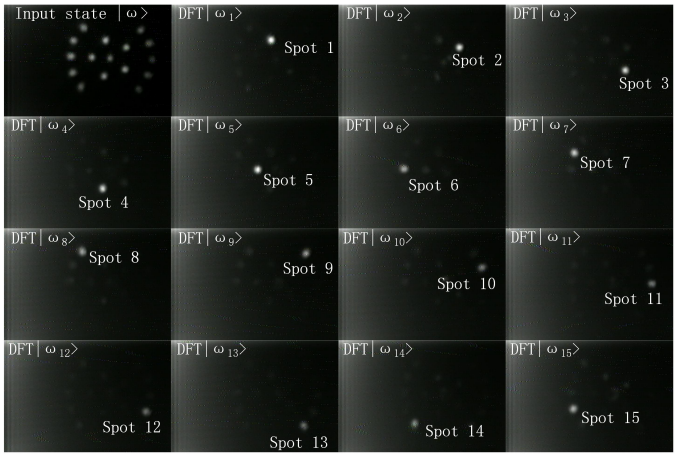

FIG. 7. The results of calibrated DFT matrix under Fourier basis. For different input Fourier states, the output of DFT matrix would be single Gaussian spots in different positions.

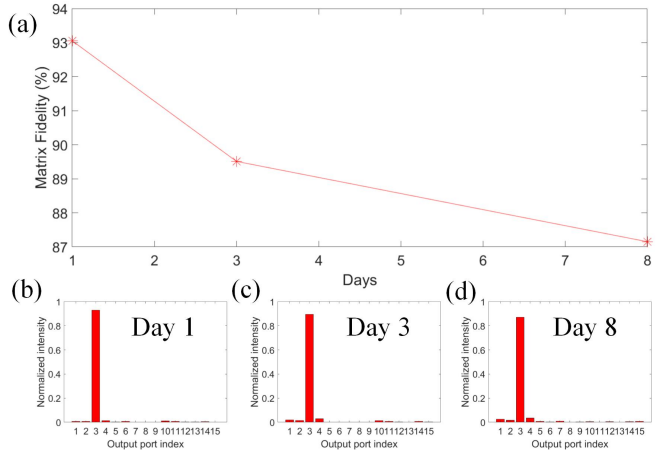

FIG. 8. (a) Matrix fidelity variation of calibrated 15×15 DFT demonstration over one week. (b∼d) The output vector of DFT with the input Fourier basis state $|\omega_3\rangle$.

It is possible to handle these phase differences among the matrix rows, via a different method for phase measurement is introduced in our previous work [29], where a reference field is required. However, the tomographic method utilized in this work is simpler and more accurate. The test results of the calibrated DFT matrix acting on the Fourier basis are shown in Fig. 7. The input and output state vectors are captured by CCD camera. All the input Fourier bases of $|\omega_n\rangle$ have uniform amplitude but different phase distributions. For different input Fourier basis states, the output of DFT matrix would be single Gaussian spots in different positions. Each time only one output port is bright while other output ports vanish due to multiport interference, as they should. The stability of our calibration method is tested over a period of one week. The fidelity of 15×15 DFT demonstration is selected as an example. As is shown in Fig. 8, the fidelity drops from $\sim$ 93% to $\sim$ 87% after 7 days with no further calibration. Once the calibration is performed, because the constant phase error is independent of the transformation matrices, any target matrices can be readily implemented with high fidelity.

Appendix B: Error analysis

The errors can be categorized as follows: (a) errors introduced by the time correlated single photon counting (TCSPC), (b) errors in design and implementation of modulation functions on SLMs and (c) imperfections in matrix calibration. Among these, the dominant one is introduced by the TCSPC due to the Poissonian counting statistics and dark counts in the detector. The errors of the parameters in SLM modulation functions as well as imperfections in matrix calibration only lead to a small loss of fidelity for the implemented linear operators and projectors.

1. Errors induced by TCSPC

The raw photon counting rate of the heralded single photon source is about 270 Hz with the IDQ220 detectors. However, the total insertion loss of experimental setup is ∼32dB including polarization control, high-dimensional state generation, linear operation and free space to fiber coupling. In addition to the intrinsic loss of 13.76 dB to implement 15×15 matrix, there is an extra loss of 7.52 dB caused by the non-unit modulation efficiency of SLM1 and SLM2. Further, additional losses of 3.01 dB, 4.46 dB and 4.15 dB are induced by polarization control as well as fiber to free space collimation, state generation with SLM0 and free space to fiber collection, respectively. As is shown in the main text, the data accumulating time for each measurement is one minute, hence only tens of coincidence events can be recorded. As the single photon events follow the Poissonian distribution, the uncertainty is $\sim \sqrt{N_{\text{count}}}$ for data series. When N_{count} is low, the relative uncertainty of coincidence counting arises and has proven to be the main reason for fidelity deterioration in our quantum projective measurements. To further confirm this, we have performed high-dimensional state tomography with the same projective method but with a classical coherent light source in place of our SPDC source. The results for symmetric informationally complete positive operator-valued measurements (SIC POVMs) as well as reconstruction of density matrices are presented in Fig. 10 in appendix C. For four groups of experiments, the statistical fidelity values of SIC POVMs are $0.979 \sim 0.996$, while the fidelity values of density matrices are $0.930 \sim 0.994$. With an intense light source, the decrease in the errors is clear. This supports our conclusion that the uncertainty of coincidence counting is the critical error in this demonstration.

The compressed sensing technique would further amplify the uncertainties. According to compressed sensing theory [37], the error ε_{DM} of reconstructed density matrix follows

$$\varepsilon_{DM} \geq \left(\sqrt{N^2/m}\right) \varepsilon_p \tag{B1}$$

N is the dimensionality of density matrix, while m is the number of projective measurements. ε_p represents errors of projection values. As the sampling ratio is about 0.35 in this work, the errors of density matrices would be at least ~ 1.7 times of errors of raw projection data, which could explain the fidelity deterioration from quantum projection values to density matrices.

The accidental coincidence rate caused by dark counts in the single photon detectors is measured to be ~ 2 per minute. The fidelity deterioration of the DFT results in the main text is caused mainly by dark counts occurring in those output ports that should be quenched due to destructive interference of a single photon.

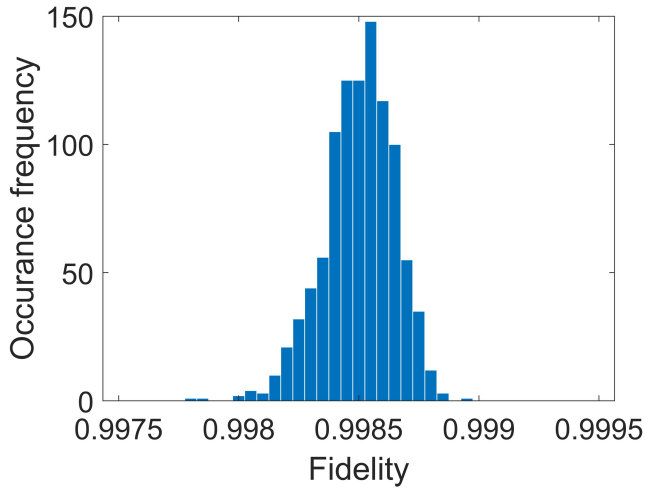

FIG. 9. The histogram for normalized fidelity of different unitary matrices with dimensionality of 15×15. The phase gratings are not optimized in these designs. The histogram is obtained through Monte Carlo simulation with 1000 trials.

2. Errors induced by modulation functions on SLMs

In principle, the phase-only modulation functions should be modified by optimization parameters of μ_{mn} and ν_{mn} in Eq. (A6) and Eq. (A9) in order to achieve unit fidelity. However, it is highly time-consuming to optimize the phase gratings every time for different tasks and after phase calibration. Moreover, as mentioned in the main text, a near unit fidelity value can be achieved even by directly setting $\{\mu_{mn}\}$ and $\{\nu_{mn}\}$ to 1. This allows fast design of phase modulation functions to realize a general target matrix, if the fidelity deterioration induced can be neglected.

To quantify the influence of optimization parameters, we have mathematically modeled our experimental setup so that it can be simulated according to the Huygens-Fresnel theorem within the paraxial approximation. In this way, we can characterize the theoretical fidelity of matrix transformations under all the experimental conditions including beam splitting, beam recombining, free space propagation and spatial filtering. 1000 unitary matrices have been randomly generated with the dimensionality of 15×15. The phase modulation functions for these matrices are designed according to Eq. (A6) and Eq. (A9) with all the optimization parameters equal to 1. Fig. 9 presents the fidelity histogram of 1000 numerical simulation trials. The standard derivation of fidelity is calculated as $\delta F < 1.5 \times 10^{-4}$. The high fidelity values and small fidelity derivation suggest that the fidelity deterioration without optimization is negligible.

3. Errors induced by matrix calibration

Matrix calibration is performed with a laser source centered at 1550 nm, which is close to the central wavelength of signal filter for single photons, which is 1549.3 nm. As SLMs are not narrow-band devices, these two wavelengths can be considered as the same for the purposes of phase calibration.

During phase calibration, the amplitudes of matrix elements are supposed to be accurate. The simulated results shown in Fig. 9 support this assumption. The intensities of output states are measured by an InGaAs CCD camera. The nonlinear effects as well as background noises of CCD camera would also induce some errors, which are mostly responsible for the fidelity difference of experimental results with intensive light presented in Fig. 10.

Appendix C: Additional tomography results

The experimental results for state tomography with classical laser source are presented in Fig. 10. Compressed sensing quantum state tomography results with different sampling ratio are displayed in Fig. 11. Figure. 10 presents four groups of experimental results. The three columns in Fig. 10 indicate results of SIC POVMs, experimental density matrices and theoretical density matrices, respectively. Figure. 10(a) presents characterization for the single-mode eigenstate, while Fig. 10(b∼d) are those of superposed states. For Fig. 10 (a∼d), the statistical fidelity values of SIC POVMs are 0.996, 0.985, 0.979 and 0.981, while the fidelity values for state tomography are 0.994, 0.946, 0.930 and 0.940.

[1] J.-W. Pan, Z.-B. Chen, *et al.*, Rev. Mod. Phys. **84**, 777 (2012).
[2] P. G. Kwiat, K. Mattle, *et al.*, Phys. Rev. Lett. **75**, 4337 (1995).
[3] A. Mair, A. Vaziri, *et al.*, Nature **412**, 313 (2001).
[4] M. Kues, C. Reimer, *et al.*, Nature **546**, 622 (2017).
[5] M. Reck, A. Zeilinger, *et al.*, Phys. Rev. Lett. **73**, 58 (1994).
[6] A. Babazadeh, M. Erhard, *et al.*, Phys. Rev. Lett. **119**, 180510 (2017).
[7] H.-H. Lu, J. M. Lukens, *et al.*, Phys. Rev. Lett. **120**, 030502 (2018).
[8] J. Bavaresco, N. Herrera Valencia, C. Klöckl, *et al.*, Nature Phys **14**, 1032 (2018).
[9] J. Wang, S. Paesani, *et al.*, Science **360**, 285 (2018).
[10] T. Brougham, C. F. Wildfeuer, *et al.*, Eur. Phys. J. D **70**, 214 (2016).
[11] E. Knill, Phys. Rev. A **66**, 052306 (2002).
[12] J. Carolan, C. Harrold, *et al.*, Science **349**, 711 (2015).
[13] P. Imany, J. A. Jaramillo-Villegas, M. S. Alshaykh, *et al.*, npj Quantum Inf **5**, 59 (2019).

[14] A. Martin, T. Guerreiro, A. Tiranov, *et al.*, Phys. Rev. Lett. **118**, 110501 (2017).
[15] A. Rossi, G. Vallone, A. Chiuri, F. De Martini, and P. Mataloni, Phys. Rev. Lett. **102**, 153902 (2009).
[16] C. K. Law and J. H. Eberly, Phys. Rev. Lett. **92**, 127903 (2004).
[17] M. V. Fedorov, Phys. Rev. A **93**, 033830 (2016).
[18] H. Wang, Y. He, Y.-H. Li, *et al.*, Nature Photon **11**, 361 (2017).
[19] N. C. Harris, G. R. Steinbrecher, *et al.*, Nature Photon **11**, 447 (2017).
[20] S. Franke-Arnold, S. M. Barnett, *et al.*, Phys. Rev. A **65**, 033823 (2002).
[21] J. Leach, B. Jack, *et al.*, Science **329**, 662 (2010).
[22] M. J. Padgett and R. W. Boyd, Phil. Trans. R. Soc. A **375**, 20160233 (2017).
[23] L. Neves, G. Lima, *et al.*, Phys. Rev. Lett. **94**, 100501 (2005).
[24] A. C. Dada, J. Leach, *et al.*, Nature Phys **7**, 677 (2011).
[25] J. Schneeloch, C. C. Tison, M. L. Fanto, P. M. Alsing, and G. A. Howland, Nat Commun **10**, 2785 (2019).
[26] F. Brandt, M. Hiekkamäki, *et al.*, arXiv:1907.13002 [physics, physics:quant-ph] (2019), arXiv:1907.13002 [physics, physics:quant-ph].
[27] S. J. B. Yoo, B. Guan, and R. P. Scott, Microsyst Nanoeng **2**, 16030 (2016).
[28] Y. Wang, V. Potoček, *et al.*, Phys. Rev. A **95**, 033827 (2017).
[29] P. Zhao, S. Li, *et al.*, J. Opt. **21**, 104003 (2019).
[30] L. A. Romero and F. M. Dickey, in *Progress in Optics*, Vol. 54 (Elsevier, 2010) pp. 319–386.
[31] L. A. Romero and F. M. Dickey, J. Opt. Soc. Am. A **24**, 2280 (2007).
[32] W. R. Clements, P. C. Humphreys, and other, Optica **3**, 1460 (2016).
[33] H. Takesue and K. Inoue, Phys. Rev. A **72**, 041804 (2005).
[34] D. F. V. James, P. G. Kwiat, *et al.*, Phys. Rev. A **64**, 052312 (2001).
[35] N. Bent, H. Qassim, *et al.*, Phys. Rev. X **5**, 041006 (2015).
[36] A. J. Scott and M. Grassl, Journal of Mathematical Physics **51**, 042203 (2010).
[37] D. Gross, Y.-K. Liu, *et al.*, Phys. Rev. Lett. **105**, 150401 (2010).
[38] M. A. Nielsen and I. L. Chuang, 10th ed. (Cambridge University Press, Cambridge ; New York, 2010).
[39] S. M. Barnett, *Quantum Information*, Oxford Master Series in Physics. Atomic, Optical and Laser Physics No. 16 (Oxford University Press, Oxford, 2009) oCLC: ocn316430129.
[40] P. W. Shor, SIAM Rev. **41**, 303 (1999).
[41] F. Wang, M. Erhard, *et al.*, Optica **4**, 1462 (2017).
[42] C.-Y. Lu, D. E. Browne, T. Yang, and J.-W. Pan, Phys. Rev. Lett. **99**, 250504 (2007).
[43] N. K. Fontaine, R. Ryf, *et al.*, Nat Commun **10**, 1865 (2019).
[44] M. Faraji-Dana *et al.*, Nat Commun **9**, 4196 (2018).
[45] A. Steane, Rep. Prog. Phys. **61**, 117 (1998).
[46] A. Politi, J. C. F. Matthews, and J. L. O'Brien, Science **325**, 1221 (2009).
[47] C. H. Bennett, G. Brassard, C. Crépeau, R. Jozsa, A. Peres, and W. K. Wootters, Phys. Rev. Lett. **70**, 1895 (1993).

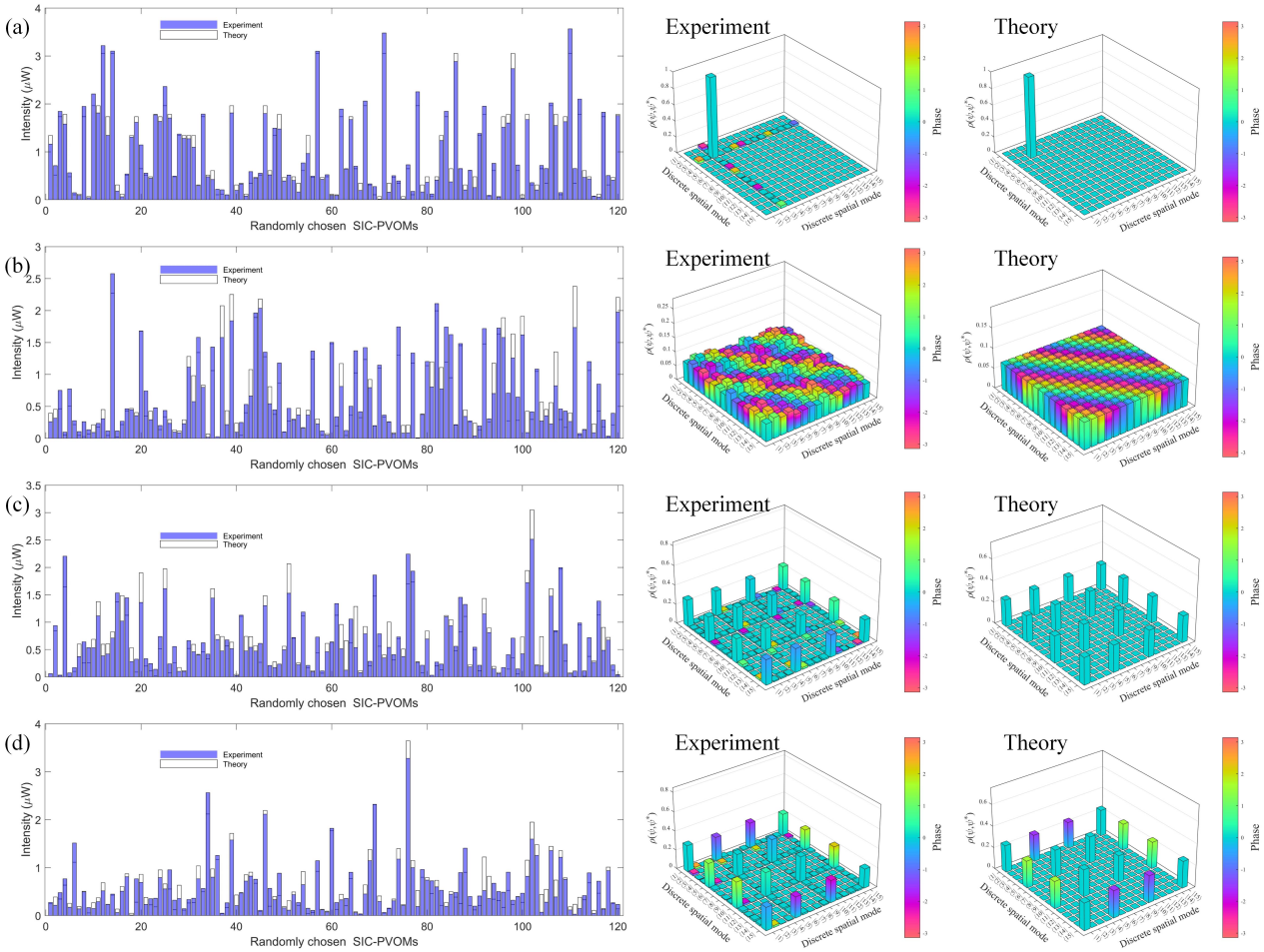

FIG. 10. (a) Four groups of state tomography with a classical coherent light source. Three columns are corresponding to the results of SIC POVMs, experimental density matrices, and theoretical density matrices, respectively. (a) Results for a single-mode eigenstate. (b∼d) Results of superposed states. The phase information for matrix elements with module $|\rho_{ij}| < 0.02$ is approximately randomly distributed and not displayed to aid clarity.

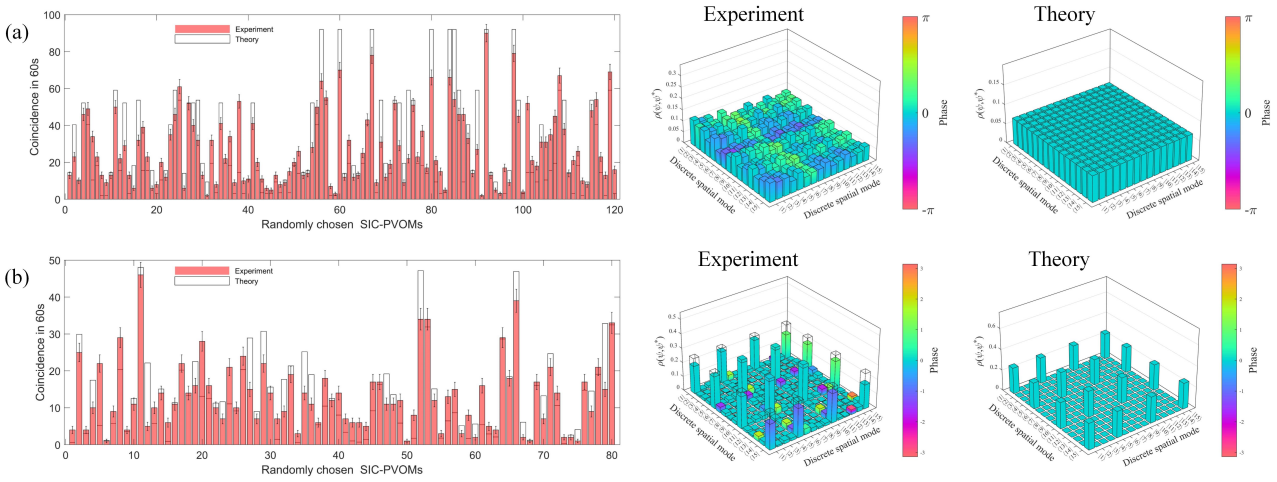

FIG. 11. Two groups of quantum projective measurements and quantum state tomography. Three columns are corresponding to the results of SIC POVMs, experimental density matrices, and theoretical density matrices, respectively. The statistical fidelity values of SIC POVM are 0.934 and 0.936 for (a) and (b), respectively. The fidelity values of quantum state tomography are 0.806 and 0.738.